Chemical Science

ROYAL SOCIETY OF CHEMISTRY

EDGE ARTICLE

View Article Online
View Journal | View Issue

Check for updates

Cite this: *Chem. Sci.*, 2023, **14**, 5656

All publication charges for this article have been paid for by the Royal Society of Chemistry

Steric hindrance-induced selective growth of rhodium on gold nanobipyramids for plasmon-enhanced nitrogen fixation†

Henglei Jia, ‡[a] Fan Li,‡[a] Yuanyuan Yang,[a] Mengxuan Zhao,[a] Jingzhao Li[a] and Chun-yang Zhang *[ab]

Received 6th January 2023
Accepted 30th April 2023

DOI: 10.1039/d3sc00081h

rsc.li/chemical-science

The construction of an antenna–reactor plasmonic photocatalyst that is composed of a plasmonic and a catalytically active metal holds great promise in driving N_2 photofixation, but its photocatalytic performance is highly dependent on the spatial distribution of the two components. Up to now, the fabrication of dumbbell-shaped nanostructures featuring spatially separated architecture has remained challenging. Herein, we develop a facile synthetic strategy for the site-selective growth of a Rh nanocrystal ‘reactor’ on two tips of an Au nanobipyramid (NBP) ‘antenna’ through the precise manipulation of steric hindrance toward Rh overgrowth. The obtained Au NBP/tip-Rh nanodumbbells (Au NBP/tip-Rh NDs) can function as an excellent antenna–reactor plasmonic photocatalyst for N_2 photofixation. In this scenario, the Au nanoantenna harvests light and generates hot electrons under plasmon resonance, meanwhile the hot electrons are transferred to the active sites on Rh nanocrystals for N_2 reduction. In comparison with that of classical core@shell nanostructures, the spatially separated architecture of the Au NBP/tip-Rh NDs facilitates charge separation, greatly improving the photocatalytic activity. This study sheds new light on the structure–function relationship for N_2 photofixation and benefits the design and construction of spatially separated plasmonic photocatalysts.

Introduction

N_2 fixation, the conversion of naturally abundant N_2 to NH_3, is an essential process in modern society because NH_3 is a fundamental building block for the synthesis of fertilizers and industrial chemical stock.[1–3] NH_3 is emerging as an alternative hydrogen carrier due to its properties of high hydrogen capacity (17.6 wt%), low liquefaction pressure (~8 atm), and ease of storage and transportation.[4] Although N_2 accounts for about 78% of the Earth's atmosphere, the direct utilization of N_2 remains challenging because N_2 is extremely stable with a N≡N bond dissociation energy of 941 kJ mol^{-1} and a large energy gap of 10.82 eV between the HOMO and LOMO.[5] NH_3 synthesis is industrially accomplished by the energy and carbon-intensive Haber–Bosch process, which results in large energy consumption and CO_2 emissions. Therefore, the development of a zero-carbon emission NH_3 synthetic strategy is highly desired. Artificial photosynthesis of NH_3 by using renewable solar energy and H_2O as the energy and proton sources has provoked much attention recently,[6–11] but traditional photocatalysts are hampered by their weak interaction with N_2 and a large reaction activation barrier. Theoretically, transition metal-based catalysts, such as Ru, Rh, and Re, are the most promising materials for N_2 fixation.[12] When a N_2 molecule interacts with a transition metal catalyst, N_2 donates electrons from its bonding orbitals to the metal and accepts electrons into its antibonding orbitals, known as back donation.[13] This back donation effect can weaken the N≡N bond and facilitate the cleavage of N_2. However, the poor light-harvesting capability of these transition metal-based catalysts limits their applications in N_2 photofixation.

The construction of antenna–reactor photocatalysts through the integration of a catalytically active metal with a strongly light-harvesting plasmonic metal holds great promise for both efficient light harvesting and high catalytic activity.[14–17] Plasmonic metal nanocrystals (*e.g.*, Au, Ag, and Cu) possess localized surface plasmon resonance (LSPR) property, which arises from the collective oscillations of free electrons confined in metal nanocrystals under resonant excitation.[18–20] LSPR can give rise to a strong electromagnetic field at the nanoscale and thereafter enhance the light-matter interaction of metal nanocrystals. More importantly, plasmonic hot electrons and holes are generated through plasmon excitation decay.[18] These energetic charge carriers are readily transferred to adjacent metals or directly utilized for chemical reactions. Among various plasmonic noble metal nanocrystals, Au

---

[a] *College of Chemistry, Chemical Engineering and Materials Science, Shandong Normal University, Jinan 250014, China. E-mail: cyzhang@sdnu.edu.cn*

[b] *School of Chemistry and Chemical Engineering, Southeast University, Nanjing 211189, China. E-mail: zhangcy@seu.edu.cn*

† Electronic supplementary information (ESI) available. See DOI: https://doi.org/10.1039/d3sc00081h

‡ These authors contributed equally to this work.

NBPs have recently received increasing attention owing to their unique architecture and the presence of high-index facets.[21–25] Therefore, the integration of Au NBPs with catalytically active metals (*e.g.*, Rh) for N_2 reduction holds great promise for driving N_2 photofixation under ambient conditions.

Precisely manipulating the architecture of bimetallic nanocrystals is of great importance to their photocatalytic performance.[26–28] In comparison with traditional core@shell nanostructures, spatially separated nanoarchitectures are more attractive, because they allow hot charge carriers to take part in reduction and oxidation reactions at different active sites independently.[29–31] Among different types of spatially separated architectures, dumbbell-shaped nanostructures offer significant benefits for charge separation in the photocatalytic N_2 reduction process.[32–38] As revealed by theoretical calculations, the sharp tips of Au NBPs can generate extremely large local electric field enhancement and the deposition of catalytically active metals at the hotspots is beneficial for the photocatalytic reaction.[21,39] Despite much promise, selective growth of Rh nanocrystals on two tips of Au NBPs remains challenging due to the lack of a wet-chemistry synthesis method.

In this work, we present a facile method for the selective growth of Rh nanocrystals on two tips of Au NBPs to fabricate Au NBP/tip-Rh NDs. The formation of a large steric hindrance at the middle of Au NBPs is vital for selective growth, which is achieved by employing benzyldimethylhexadecylammonium chloride (16-BAC) molecules as the surfactant. Since Rh nanocrystals tend to aggregate in small sizes, the large benzyl group in the 16-BAC molecules presents a large steric hindrance to block the deposition of Rh on the side surface. The unique architecture endows the obtained Au NBP/tip-Rh NDs with excellent photocatalytic performance toward N_2 fixation. Benefiting from the spatially separated architecture, the Au NBP/tip-Rh NDs exhibit a N_2 photofixation activity of 114.33 μmol h^{-1} g^{-1}, which is 8.0 and 2.0-fold compared with those of Rh nanocrystals and core@shell nanostructures.

Results and discussion

The Au NBP/tip-Rh NDs are prepared through the selective growth of Rh nanocrystals on two tips of Au NBPs (Fig. 1). The pregrown Au NBPs are stabilized with the surfactant cetyltrimethylammonium bromide (CTAB) molecules. In the absence of 16-BAC, Rh nanocrystals are prone to nucleation on the whole surface of Au NBPs to obtain the core@shell nanostructures. Since Rh nuclei are generally very small, the small steric hindrance of CTAB molecules can hardly prevent the deposition of Rh nuclei on the side surface, and subsequently core@shell nanostructures are formed. 16-BAC molecules have a similar molecular structure to CTAB. A big difference lies in that 16-BAC molecules possess a large benzyl headgroup but CTAB molecules have a small methyl group. The presence of 16-BAC molecules facilitates the selective growth process. First, the large headgroup of 16-BAC molecules can block the entrance of Rh nuclei into the side surfaces of Au NBPs. At an appropriate concentration, the density of 16-BAC molecules at the two tips is smaller than that on the side surface due to the curvature difference,[34] which provides an opportunity for Rh nucleation at the two tips. Second, 16-BAC has a stronger capability of stabilizing the Rh precursor than CTAB due to the larger headgroup. The strong bonding capability reduces the number of nucleations and slows down the growth rate of Rh. Upon the nucleation of Rh nanocrystals at the two tips, further deposition of Rh will occur on the original Rh nuclei because of the smaller interfacial free energy than the Au–Rh interface. In addition, the presence of NaI during the synthesis facilitates the epitaxial overgrowth of Rh on Au NBP.[40] First, the complexation of I^- ions with Rh^{3+} ions can decrease the nucleation rate of Rh nanocrystals by decreasing the reduction potential. Second, the I^- ions possess strong interaction with Au, which can direct the growth of Rh on Au NBPs. Third, the presence of the I^-/I_2 red/ox pair makes I^- ions a good candidate as a reduction/oxidation agent for the activation of the Au surface. Accordingly, Rh nanodomains are formed at two tips of Au NBPs to obtain the Au NBP/tip-Rh NDs.

The starting Au NBPs with a fivefold rotational symmetry structure were prepared using a seeded growth method (Fig. 2a). The as-prepared Au NBPs possess a uniform morphology and a narrow spectral linewidth, with the average length and diameter at the middle being 110.8 ± 2.9 nm and 35.5 ± 1.9 nm, respectively. The excellent monodispersity of Au NBPs provides an ideal platform for Rh selective growth on Au NBPs. The representative transmission electron microscopy (TEM) image of the obtained Au NBP/tip-Rh NDs clearly demonstrates that Rh nanocrystals have been successfully grown on two tips of Au NBPs (Fig. 2b). The Rh nanocrystals exhibit a snowflake morphology with a diameter of 36.9 ± 3.2 nm and are composed of many small dendritic Rh nanostructures (Fig. 2c). After the growth of Rh nanocrystals, a redshift for plasmon resonance wavelength occurs due to the change of the dielectric constant at the two tips (Fig. S1†). To further verify the dumbbell-shaped nanostructures, we carried out high-angle annular dark-field scanning transmission electron microscopy (HAADF-STEM) imaging and energy-dispersive X-ray (EDX) elemental mapping (Fig. 2d). Evidently, the EDX elemental mapping results reveal the bipyramidal Au core and well-defined Rh nanodendrite-tipped caps, suggesting the formation of dumbbell-shaped nanostructures. In addition, the crystalline properties of Au and Rh are confirmed by aberration-corrected high-resolution TEM (HRTEM) imaging (Fig. 2e). An aberration-corrected HRTEM image clearly demonstrates that the Rh cap consists of many dendritic nanostructures with a diameter of about 1–3 nm. The formation of dendritic structures is attributed to the large lattice mismatch (~7%) between Au and Rh.[40] Dendritic nanostructures with porous channels of Rh nanocrystals are supposed to be ideal architectures for catalysis.

To examine the structure and composition of the Au NBP/tip-Rh NDs, we performed X-ray diffraction (XRD) and X-ray photoelectron spectroscopy (XPS) (Fig. 3). There are two sets of diffraction patterns in the XRD spectrum, consistent with the combination of standard powder diffraction patterns of Au (JCPDS #4-784) and Rh (JCPDS #5-685), suggesting the highly crystalline nature of the dumbbell-shaped structure (Fig. 3a). Analogously, the survey XPS spectrum further confirms the

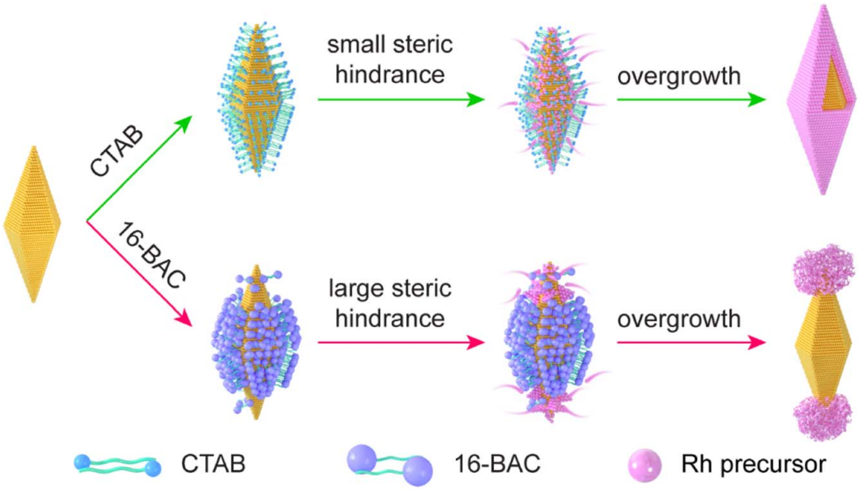

Fig. 1 Schematic illustration of the growth behaviors of Rh nanocrystals on Au NBPs in the presence of either CTAB or 16-BAC surfactants.

presence of Au and Rh in the Au NBP/tip-Rh ND sample (Fig. S2†). The high-resolution Au 4f XPS spectrum presents two strong peaks located at 83.8 eV (Au $4f_{7/2}$) and 87.5 eV (Au $4f_{5/2}$), suggesting the metallic Au^0 state (Fig. 3b).[24] The Rh 3d XPS spectrum can be fitted with four peaks (Fig. 3c). Two peaks (307.1 eV and 311.9 eV) originate from the Rh^0 state, while the other two peaks (308.1 eV and 313.1 eV) are assigned to the Rh^{3+} state.[41,42] The Rh^0/Rh^{3+} ratio is 54 : 46 calculated by integrating the peak areas. The appearance of Rh^{3+} peaks arises from the surface oxidation of the dendritic Rh nanocrystals,[42] because

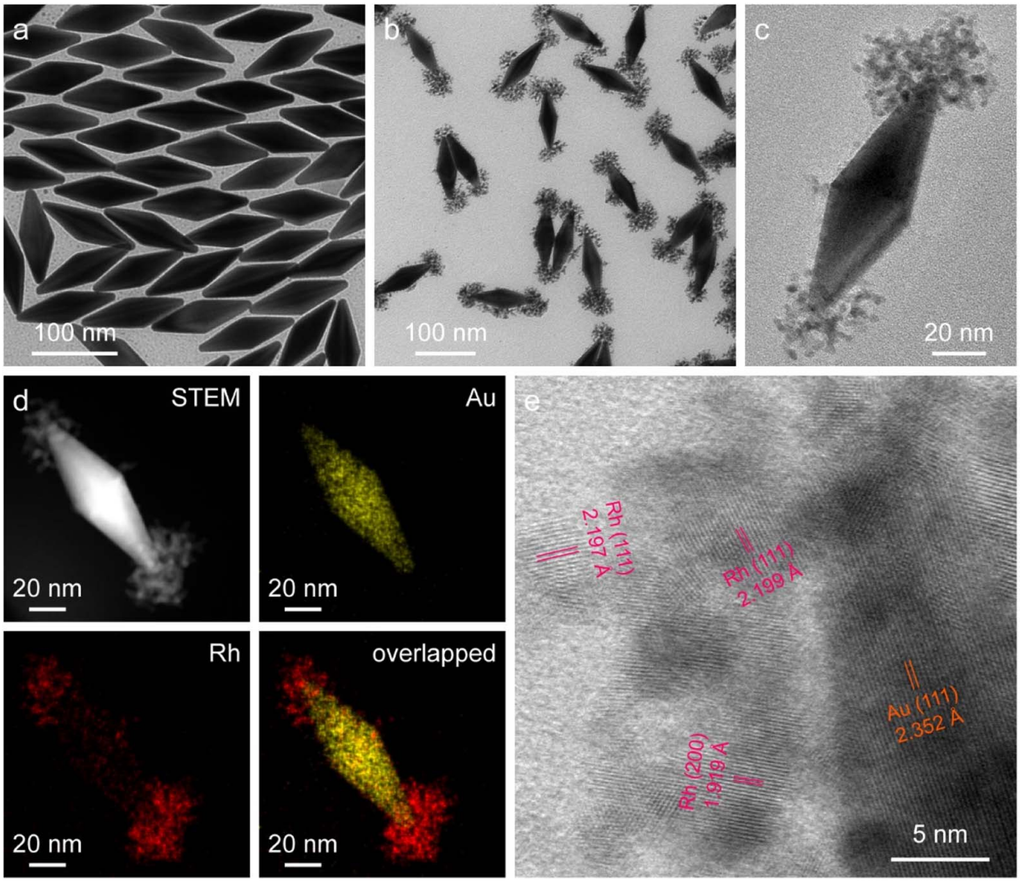

Fig. 2 Dumbbell-shaped Au/Rh nanostructures. (a and b) TEM images of the Au NBPs (a) and Au NBP/tip-Rh NDs (b). (c) TEM image of a representative Au NBP/tip-Rh ND. (d) HAADF-STEM image and the corresponding EDX elemental maps of a single Au NBP/tip-Rh ND. (e) Aberration-corrected HRTEM image at the Au–Rh interface.

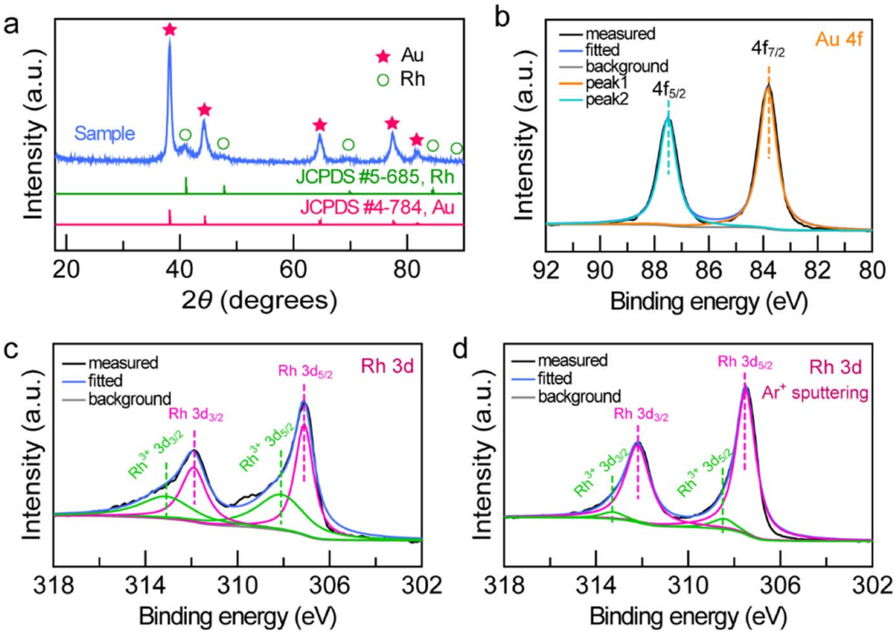

Fig. 3 Structure and chemical composition of the Au NBP/tip-Rh NDs. (a) XRD patterns. (b) High-resolution Au 4f XPS spectrum. (c and d) High-resolution Rh 3d XPS spectra before (c) and after (d) the Ar^+ ion sputtering experiments.

XPS is only sensitive to the surface of materials.[10] After the Ar^+ ion sputtering, the Rh^0/Rh^{3+} value is 92/8 (Fig. 3d), indicating that the dominant form of Rh is metallic Rh.

The unique dumbbell-shaped architecture of the Au NBP/tip-Rh NDs holds great promise for driving N_2 photofixation as an antenna–reactor photocatalyst. To evaluate the photocatalytic performance of the dumbbell-shaped nanostructures, we performed N_2 fixation experiments under visible-NIR light ($\lambda > 420$ nm) illumination (Fig. S3†). To close the photocatalytic cycle, methanol was employed as the hole scavenger. For better comparison, we prepared four other catalysts, including pure Au NBPs, Rh nanocrystals (Fig. S4 and S5†), a mixture of Au NBPs with Rh nanocrystals, and Au NBP@Rh core@shell nanostructures (Fig. S4†). The exact weights of the photocatalysts were determined by inductively coupled plasma optical emission spectroscopy (ICP-OES) (Fig. S6 and Table S1†). Prior to the N_2 fixation experiments, a linear calibration relationship was first precalibrated, and the generated NH_3 amounts were determined by the indophenol-blue method (Fig. S7†).

The spatially separated design of dumbbell-shaped nanostructures is advantageous for charge separation and may serve as an ideal platform for the study of structure–function relationship. As displayed in Fig. 4a, the generated NH_3 amounts on different catalysts gradually increase with the illumination time, suggesting that NH_3 originates from the photocatalytic reduction of N_2. The Au NBP and Rh nanocrystal samples exhibit very weak photocatalytic activities due to the lack of active sites or poor light-harvesting capability. The improvement of the N_2 fixation activity is small by simply mixing the Au NBPs with Rh nanocrystals, suggesting that the antenna–reactor mechanism does not function without direct contact through a sharing interface. Impressively, the Au NBP/tip-Rh NDs exhibit a superior photocatalytic activity toward N_2 fixation. The N_2 fixation rate of the Au NBP/tip-Rh NDs is 114.33 μmol h^{-1} g^{-1}, which is 8.0 and 2.0-fold compared with those of Rh nanocrystals and the core@shell nanostructures (Fig. 4b). The improvement in the photocatalytic performance is ascribed to the spatially separated architecture of the dumbbell-shaped nanostructures. To gain more insight, we carried out photocurrent measurements at the open-circuit potential to investigate the charge separation in the dumbbell-shaped and core@shell nanostructures. As displayed in Fig. S8†, the photocurrent generated by the dumbbell-shaped nanostructures is 2.1-fold higher than that generated by the core@-shell nanostructures, suggesting that the spatially separated architecture facilitates charge separation in the photocatalytic process. Control experiments confirm that there is no NH_3 production under these conditions: (a) without catalysts, (b) without illumination, and (c) replacement of N_2 with Ar as the feeding gas, suggesting that the product NH_3 originates from the photocatalytic reduction of N_2 on the Au NBP/tip-Rh NDs (Fig. S9†). The NH_3 generation rate drops to 45.4% (51.9 ± 17.3 μmol h^{-1} g^{-1}) in the absence of the sacrificial agent, implying the importance of the sacrificial agent in N_2 fixation. To further trace the source of NH_3, we carried out the isotope labelling experiments by conducting N_2 fixation under $^{14}N_2$ and $^{15}N_2$ atmospheres, respectively (Fig. 4c). The products in the reaction solutions were analysed using the ^1H NMR spectrum. Under a $^{14}N_2$ atmosphere, triple peaks appear in the ^1H NMR spectrum, consistent with the peaks of standard $^{14}NH_4Cl$ solution. When $^{15}N_2$ is employed as the nitrogen source, only double peaks are detected, which are identical to those of the standard $^{15}NH_4Cl$ solution. The isotope labelling experiments further

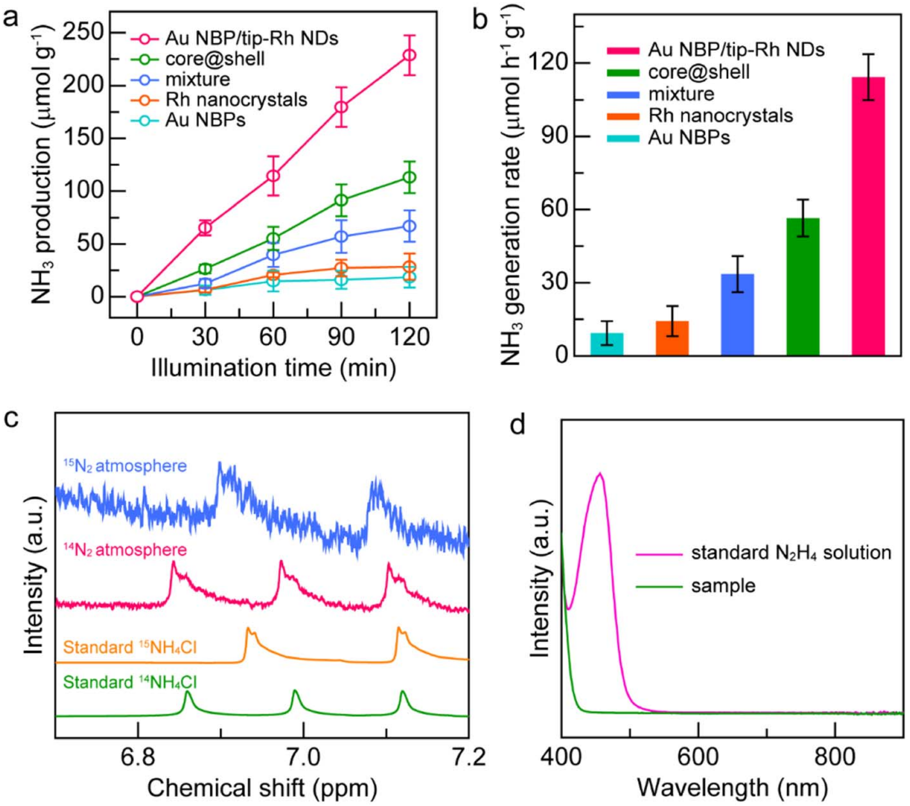

Fig. 4 N_2 photofixation under visible-NIR light illumination. (a) NH_3 productions as a function of time for different catalysts. (b) Comparison of the NH_3 production rates on different catalysts. (c) Isotope labelling experiments. (d) Detection of possible N_2H_4 in the reaction system. The standard N_2H_4 solution has an absorption peak at 455 nm.

verify that the generated NH_3 is derived from the reduction of N_2 rather than contamination or other sources. In addition, the absence of N_2H_4 in the reaction solution underlines the high selectivity of the N_2 photofixation on the Au NBP/tip-Rh NDs (Fig. 4d).

Notably, one of the great challenges in N_2 photofixation is the competition between NH_3 synthesis and H_2 evolution.[7] To further determine the selectivity of the Au NBP/tip-Rh ND photocatalyst, we performed the N_2 photofixation experiment in a gastight glass reactor under a N_2 atmosphere and analyzed the generated H_2 using an off-line gas chromatograph (Fig. S10†). The generation rate is 61.2 μmol h^{-1} g^{-1} for NH_3 and 7.8 μmol h^{-1} g^{-1} for H_2. Since $2e^-$ and $3e^-$ are required for the generation of one H_2 or one NH_3 molecule, the selectivity of NH_3 was calculated on the basis of the consumed electrons.[35] The selectivity of NH_3 is 92.2%, suggesting the presence of a competitive H_2 evolution side reaction. Even though the reduction of H_2O is the main bottleneck for NH_3 synthesis, the products are readily separated because NH_3 is highly soluble. To confirm the stability of the Au NBP/tip-Rh ND sample in the photocatalytic process, the catalyst was recovered and characterized after a typical photocatalytic reaction (Fig. S11–S13†). No obvious morphological and structural changes are observed, suggesting the excellent stability of the catalyst. Moreover, the photocatalyst exhibits good recyclability, with the photocatalytic activity remaining unchanged after three successive cycles (Fig. S14†). The contact area between the two components in the bicomponent plasmonic nanocrystals may affect the photocatalytic performance, especially in those metal/semiconductor nanostructures with a Schottky junction, because the Schottky barrier only allows hot electrons with sufficient energy to be utilized. It has been reported previously that an appropriate contact area is crucial to photocatalytic activity in the Janus Au–Cu_2O nanostructures, striking a balance between the Schottky contact area and charge dissipation.[31] In stark contrast, there is an absence of the Schottky barrier at the Au–Rh interface. Direct electron transfer from Au nanoantennas to Rh reactors can easily elevate the transfer efficiency. In addition, the plasmonic energy can transfer to the catalytic metal even if there is no direct contact between the antenna and reactor.[43] Moreover, an extremely high electromagnetic field generated at the tips and Rh nanocrystals located at the hotspots of Au NBPs are beneficial for the photocatalytic activity.

The excellent photocatalytic performance of the dumbbell-shaped nanostructures benefits from the antenna–reactor photocatalytic mechanism. To ascertain whether the photocatalytic reaction is driven by the LSPR of Au NBPs, we performed the N_2 fixation experiments under the illumination of different monochromatic lights and calculated the apparent quantum efficiencies (AQEs). Fig. 5a displays the action spectrum of the Au NBP/tip-Rh NDs for N_2 photofixation. Notably, the AQE values obtained at different wavelengths faithfully follow the absorption spectrum of Au NBPs, confirming the

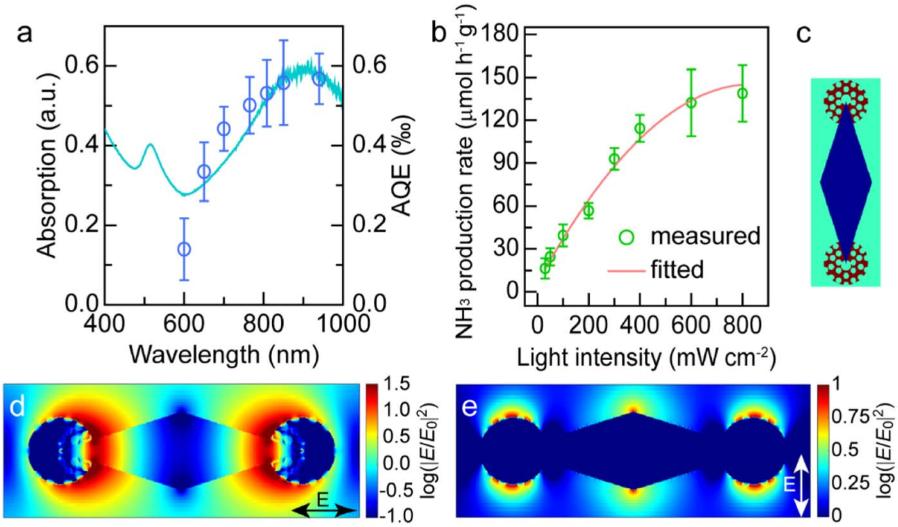

Fig. 5 Plasmon-driven N_2 photofixation. (a) Extinction (left) and AQE action (right) spectra of the Au NBP/tip-Rh NDs. (b) NH_3 generation rates under different light intensities. (c) Schematic model of the Au NBP/tip-Rh ND structure used for FDTD simulations. (d and e) FDTD-simulated electric field intensity enhancement contours under the longitudinal (c) and transverse excitations, respectively.

plasmon-driven N_2 photofixation process. Specifically, the AQE value is 0.57‰ at 940 nm, which is comparable to that of representative work on N_2 photofixation with AuRu core-antenna nanostructures as the photocatalyst.[8] The AQE action spectra also suggest that the N_2 photofixation is mainly driven by NIR light, different from those catalysts which can only harvest visible light for photocatalysis. Previous studies have shown that plasmonic nanocrystals can accelerate chemical reactions through either plasmonic photocatalysis or the photothermal heating effect.[44,45] In the N_2 photofixation experiments, the temperature of the reaction solution is kept at 25 °C by using a water-circulation cooling system. To distinguish the contribution of plasmonic photocatalysis and photothermal heating, we carried out N_2 fixation experiments in water baths set at different temperatures without illumination (Fig. S15†). In comparison with those under light illumination, the photocatalytic activities in water baths are very low. In addition, the core@shell nanostructures have the same photothermal effect as the dumbbell-shaped nanostructures, but they display lower photocatalytic activity under illumination. Although the photothermal heating effect can hardly be ruled out, these results suggest that plasmon-driven photocatalysis makes a dominant contribution to the excellent activity of the Au NBP/tip-Rh NDs.

Plasmon can drive chemical reactions *via* two classes of mechanisms including the energy transfer mechanism[43,46–48] and charge transfer mechanism.[44,45,49] We further investigated the underlying mechanism of plasmon-driven N_2 photofixation. On the one hand, we studied the dependence of the NH_3 production rate upon light intensity to corroborate the contribution of plasmonic hot electrons (Fig. 5b). An approximately linear relationship between the reaction activity and the light intensity substantiates the crucial contribution of plasmonic hot electrons to photocatalytic activity, because the linear dependence is a significant indicator for the electron-driven chemical reaction.[50,51] On the other hand, the plasmon-induced resonance energy transfer (PIRET) process can contribute to the plasmonic photocatalysis. To gain a deep insight into the contribution of the PIRET process, we carried out finite-difference time domain (FDTD) simulations to investigate the electromagnetic field enhancement around the dumbbell-shaped nanostructures (Fig. 5c–e). The representative dumbbell-shaped nanostructures were modelled on the basis of the measured geometrical parameters. The electromagnetic field distribution of the Au NBP/tip-Rh NDs was calculated at their plasmon wavelength of 900 nm in two polarization directions. As revealed by the FDTD results, the largest electromagnetic field enhancement is located at the tips of Au NBPs. The excellent photocatalytic activity of the Au NBP/tip-Rh NDs can be ascribed to the strong electromagnetic field enhancement, since the Rh reactor is just located at the hotspot of Au NBPs. The strong local field enhancement can focus light energy onto the Rh catalyst, which efficiently boosts the generation of hot charge carriers and subsequently promotes the photocatalytic activity. Consequently, both hot electron transfer and PIRET processes have significant influence on the plasmonic photocatalysis. In fact, the plasmon-driven chemical reaction is a much more complex process, and it remains elusive to differentiate the contributions of energy transfer and charge transfer to the photocatalytic activity. In future work, we should focus on the study of quantifying charge transfer and energy transfer contributions in plasmon-driven photocatalysis.

To gain a deep insight into the N_2 adsorption and activation processes on the Au NBP/tip-Rh NDs, we conducted both experimental and theoretical studies. First, to clarify the interaction of N_2 with the photocatalyst, we investigated the active sites for N_2 adsorption and activation using density functional theory (DFT) calculations (Fig. 6a–d). The adsorption energies of N_2 on Au and Rh are −0.81 eV and −1.06 eV, respectively. The more negative adsorption energy suggests that the active site for N_2 fixation is on Rh in Au NBP/Rh NDs. Such a strong interaction of N_2 with Rh facilitates the electron transfer from the active sites of Rh to N_2 molecules. To gain a deeper understanding of the N_2 activation process, we conducted low-temperature Fourier-transform infrared (LT-FTIR) experiments under Ar and N_2 atmospheres, respectively (Fig. 6e). Under the Ar atmosphere, only a negative band at 2368 cm^{-1} that corresponds to the deduction of environmental CO_2 can be detected. In contrast, an obvious vibration peak at 2248 cm^{-1} appears under the N_2 atmosphere, suggesting that the N_2 molecule chemisorbs on the catalyst *via* an end-on rather than side-on configuration to form a Rh–N_2 complex. The LT-FTIR experiments clearly confirm the activation process of N_2 on the Au NBP/Rh NDs. After identifying the Rh active sites, we further investigated the reaction pathways of N_2 reduction on the Au NBP/tip-Rh ND catalyst by using DFT calculations. The reduction of N_2 to NH_3 can go through three classes of pathways including dissociative, distal, and alternating pathways.[52] Since the dissociative pathway requires a large amount of energy to break the N≡N triple bond, the N_2 reduction reaction is generally conducted at high temperatures and high pressures (*e.g.*, the traditional Haber–Bosch process). We calculated the Gibbs free energy changes in the alternating and distal pathways on the Au NBP/tip-Rh ND catalyst. As displayed in Fig. 6f, the rate-determining steps in alternating and distal pathways are both the desorption of the first NH_3 from the Au NBP/Rh NDs. The uphill energy is 0.67 eV for the alternating pathway and 0.50 eV for the distal pathway, revealing that the distal pathway is the most favourable path for N_2 reduction on the Au NBP/tip-Rh NDs. In addition, the calculation results corroborate the fact that there is an absence of byproduct N_2H_4 in this system. It has been reported that the desorption of $*NH_2NH_2$ to obtain byproduct N_2H_4 is a highly endothermic step.[53] As a competitive reaction, the further hydrogenation of $*NH_2NH_2$ on the Au NBP/tip-Rh NDs is exothermic, suggesting that NH_3

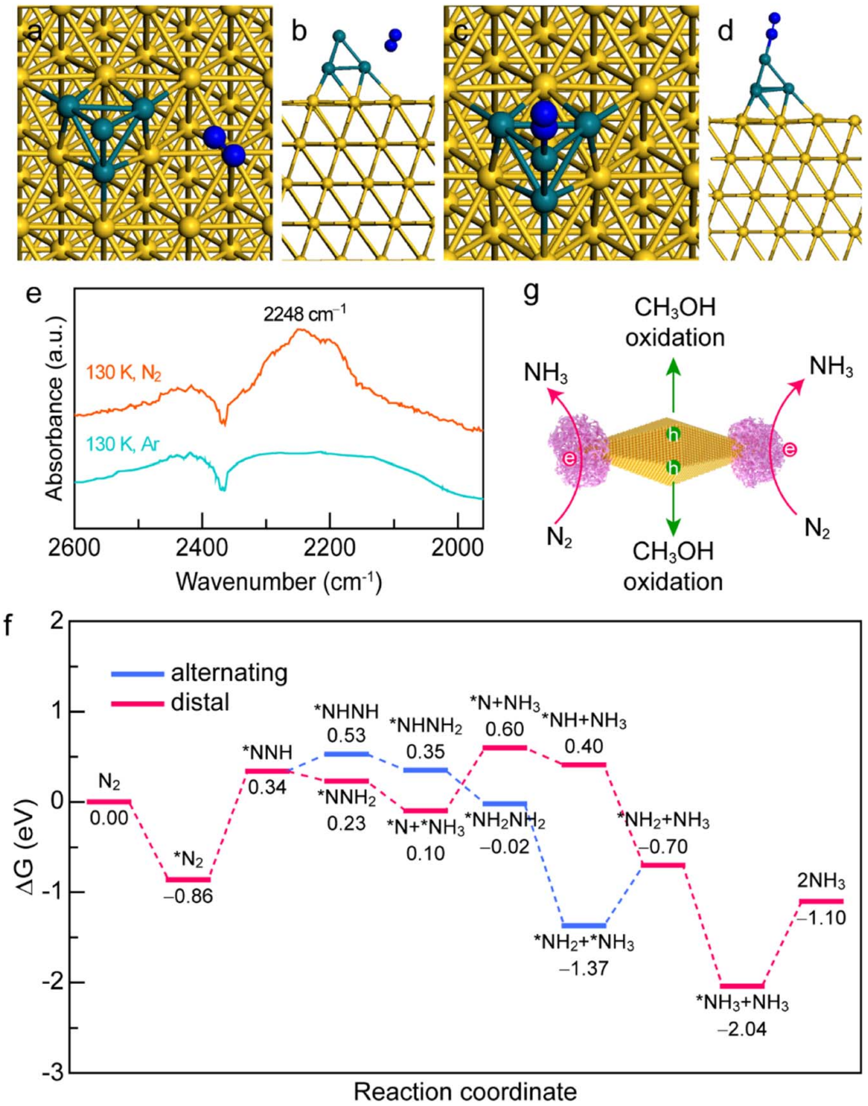

Fig. 6 Mechanism for N_2 photofixation on Au NBP/tip-NDs. (a and b) N_2 adsorption on Au in the Au NBP/tip-Rh NDs (top view (a) and side view (b)). (c and d) N_2 adsorption on Rh in the Au NBP/tip-Rh NDs (top view (c) and side view (d)). (e) LT-FTIR spectra of the Au NBP/tip-Rh NDs under Ar and N_2 atmospheres, respectively. (f) Gibbs free-energy diagrams of the N_2 photofixation on the Au NBP/tip-Rh NDs through alternative and distal pathways. (g) Schematics illustrating the charge carrier separation behaviour in the Au NBP/tip-Rh NDs.

rather than N_2H_4 is more readily generated in this photocatalytic system.

Based on the above experimental and theoretical results, a rational mechanism for the N_2 photofixation on the Au NBP/tip-Rh NDs is proposed (Fig. 6g). The N_2 molecule chemisorbs on the active sites on Rh *via* an end-on configuration to form a Rh–N_2 complex. The strong interaction of N_2 molecules with the Rh catalyst weakens the N≡N triple bond and activates the N_2 molecules. Under plasmon resonance, hot electrons and holes are generated in Au NBPs. Hot electrons are transferred to the Rh catalyst for the reduction of N_2 to NH_3 *via* the associative distal mechanism, while hot holes are consumed on the side surface of Au NBPs to close the photocatalytic cycle. The antenna–reactor system combined with plasmonic Au NBPs with desired catalytically active Rh nanocrystals efficiently harnesses the light harvesting and facilitates the energy transfer from the Au NBPs to the Rh catalyst for superior N_2 photofixation. Moreover, the spatially separated architecture of the dumbbell-shaped nanostructures facilitates charge separation and promotes the catalytic performance.

Conclusions

In summary, we have developed a synthetic strategy to fabricate dumbbell-shaped Au/Rh nanostructures through the site-selective growth of Rh nanocrystals on two tips of Au NBPs. The 16-BAC molecules with a benzyl headgroup can generate a large steric hindrance at the middle of Au NBPs, facilitating the preferential nucleation of Rh at the tips and the formation of dumbbell-shaped architecture. The rational combination of plasmonic Au NBPs with desired catalytically active Rh nanocrystals to form an antenna–reactor system can not only efficiently harness the light harvesting for hot electron generation but also improve the catalytic activity toward N_2 photofixation. More importantly, the dumbbell-shaped nanostructures featuring spatially separated architecture allow hot charge carriers to take part in the reduction and oxidation half-reactions at different active sites independently, greatly enhancing the charge separation and promoting the catalytic activity. The N_2 photofixation activity of the dumbbell-shaped nanostructures is 8.0 and 2.0-fold higher compared with those of Rh nanocrystals and the core@shell nanostructures. This merit results from the rational design of the antenna–reactor system and the spatially separated architecture of the dumbbell-shaped nanostructures. Since there are also five tips at the middle of Au NBPs due to the fivefold rotational symmetry, the selective deposition of Rh at all seven tips is much more intriguing. Our future work should focus on the combination of hard templates with soft templates to fabricate 7 tip-coated Au NBPs. Above all, our study sheds new light on the precise manipulation of the active site spatial distribution in N_2 photofixation and offers instructive guidance for the design and construction of antenna–reactor plasmonic photocatalysts.

Data availability

The data that support the finding of this study are available in the main text and the ESI. †

Author contributions

H. L. Jia and F. Li contributed equally to this work. H. L. Jia and C.-y. Zhang conceived and supervised the project. F. Li performed the experiments. Y. Y. Yang, M. X. Zhao, and J. Z. Li analysed the data and provided conceptual contributions. H. L. Jia and C.-y. Zhang wrote the paper. All authors discussed the results and commented on the manuscript.

Conflicts of interest

There are no conflicts to declare.

Acknowledgements

This work was supported by the National Natural Science Foundation of China (Grant No. 21735003) and the Natural Science Foundation of Shandong Province (No. ZR2020MB040).

Notes and references

1 M.-A. Légaré, G. Bélanger-Chabot, R. D. Dewhurst, E. Welz, I. Krummenacher, B. Engels and H. Braunschweig, *Science*, 2018, **359**, 896–900.

2 M. J. Chalkley, M. W. Drover and J. C. Peters, *Chem. Rev.*, 2020, **120**, 5582–5636.

3 Y. Ohki, K. Munakata, Y. Matsuoka, R. Hara, M. Kachi, K. Uchida, M. Tada, R. E. Cramer, W. M. C. Sameera, T. Takayama, Y. Sakai, S. Kuriyama, Y. Nishibayashi and K. Tanifuji, *Nature*, 2022, **607**, 86–90.

4 J. P. Guo and P. Chen, *Chem*, 2017, **3**, 709–714.

5 C. Tang and S.-Z. Qiao, *Chem. Soc. Rev.*, 2019, **48**, 3166–3180.

6 S.-L. Meng, X.-B. Li, C.-H. Tung and L.-Z. Wu, *Chem*, 2021, **7**, 1431–1450.

7 J. H. Yang, Y. Z. Guo, R. B. Jiang, F. Qin, H. Zhang, W. Z. Lu, J. F. Wang and J. C. Yu, *J. Am. Chem. Soc.*, 2018, **140**, 8497–8508.

8 C. Y. Hu, X. Chen, J. B. Jin, Y. Han, S. M. Chen, H. X. Ju, J. Cai, Y. R. Qiu, C. Gao, C. M. Wang, Z. M. Qi, R. Long, L. Song, Z. Liu and Y. J. Xiong, *J. Am. Chem. Soc.*, 2019, **141**, 7807–7814.

9 Y. X. Zhao, Y. F. Zhao, R. Shi, B. Wang, G. I. N. Waterhouse, L.-Z. Wu, C.-H. Tung and T. R. Zhang, *Adv. Mater.*, 2019, **31**, 1806482.

10 H. Y. Bai, S. H. Lam, J. H. Yang, X. Z. Cheng, S. S. Li, R. B. Jiang, L. Shao and J. F. Wang, *Adv. Mater.*, 2022, **34**, 2104226.

11 H. L. Jia, M. X. Zhao, A. X. Du, Y. R. Dou and C.-y. Zhang, *Chem. Sci.*, 2022, **13**, 13060–13067.

12 S. Z. Andersen, V. Čolić, S. Yang, J. A. Schwalbe, A. C. Nielander, J. M. McEnaney, K. Enemark-Rasmussen, J. G. Baker, A. R. Singh, B. A. Rohr, M. J. Statt, S. J. Blair, S. Mezzavilla, J. Kibsgaard, P. C. K. Vesborg, M. Cargnello, S. F. Bent, T. F. Jaramillo, I. E. L. Stephens, J. K. Nørskov and I. Chorkendorff, *Nature*, 2019, **570**, 504–508.

13 H.-P. Jia and E. A. Quadrelli, *Chem. Soc. Rev.*, 2014, **43**, 547–564.

14 L. N. Zhou, J. M. P. Martirez, J. Finzel, C. Zhang, D. F. Swearer, S. Tian, H. Robatjazi, M. H. Lou, L. L. Dong, L. Henderson, P. Christopher, E. A. Carter, P. Nordlander and N. J. Halas, *Nat. Energy*, 2020, **5**, 61–70.

15 K. Sytwu, M. Vadail, F. Hayee, D. K. Angell, A. Dai, J. Dixon and J. A. Dionne, *Science*, 2021, **371**, 280–283.

16 D. F. Swearer, H. Q. Zhao, L. N. Zhou, C. Zhang, H. Robatjazi, J. M. P. Martirez, C. M. Krauter, S. Yazdi, M. J. McClain, E. Ringe, E. A. Carter, P. Nordlander and N. J. Halas, *Proc. Natl. Acad. Sci. U. S. A.*, 2016, **113**, 8916–8920.

17 H. L. Jia, Y. Y. Yang, Y. R. Dou, F. Li, M. X. Zhao and C.-y. Zhang, *Chem. Commun.*, 2022, **58**, 1013–1016.

18 S. Linic, P. Christopher and D. B. Ingram, *Nat. Mater.*, 2011, **10**, 911–921.

19 S. S. Li, H. Huang, L. Shao and J. F. Wang, *ACS Nano*, 2021, **15**, 10759–10768.

20 S. Q. Luo, X. H. Ren, H. W. Lin, H. Song and J. H. Ye, *Chem. Sci.*, 2021, **12**, 5701–5719.

21 T. H. Chow, N. N. Li, X. P. Bai, X. L. Zhuo, L. Shao and J. F. Wang, *Acc. Chem. Res.*, 2019, **52**, 2136–2146.

22 A. Sánchez-Iglesias, N. Winckelmans, T. Altantzis, S. Bals, M. Grzelczak and L. M. Liz-Marzán, *J. Am. Chem. Soc.*, 2017, **139**, 107–110.

23 X. Z. Zhu, H. K. Yip, X. L. Zhuo, R. B. Jiang, J. L. Chen, X.-M. Zhu, Z. Yang and J. F. Wang, *J. Am. Chem. Soc.*, 2017, **139**, 13837–13846.

24 H. L. Jia, Y. Y. Yang, T. H. Chow, H. Zhang, X. Y. Liu, J. F. Wang and C.-y. Zhang, *Adv. Funct. Mater.*, 2021, **31**, 2101255.

25 X. Z. Zhu, J. Xu, H. Zhang, X. M. Cui, Y. Z. Guo, S. Cheng, C. X. Kan and J. F. Wang, *Chem. Sci.*, 2020, **11**, 3198–3207.

26 K. D. Gilroy, A. Ruditskiy, H.-C. Peng, D. Qin and Y. N. Xia, *Chem. Rev.*, 2016, **116**, 10414–10472.

27 X. Z. Zhu, H. L. Jia, X.-M. Zhu, S. Cheng, X. L. Zhuo, F. Qin, Z. Yang and J. F. Wang, *Adv. Funct. Mater.*, 2017, **27**, 1700016.

28 J. Guo, Y. Zhang, L. Shi, Y. F. Zhu, M. F. Mideksa, K. Hou, W. S. Zhao, D. W. Wang, M. T. Zhao, X. F. Zhang, J. W. Lv, J. Q. Zhang, X. L. Wang and Z. Y. Tang, *J. Am. Chem. Soc.*, 2017, **139**, 17964–17972.

29 S.-i. Naya, T. Kume, R. Akashi, M. Fujishima and H. Tada, *J. Am. Chem. Soc.*, 2018, **140**, 1251–1254.

30 X. Q. Yang, Y. Lu, Y. Liu, J. Wang, L. Shao and J. F. Wang, *Small Struct.*, 2021, **2**, 2100101.

31 W. J. Xu, J. Jia, T. Wang, C. Li, B. W. He, J. P. Zong, Y. W. Wang, H. J. Fan, H. X. Xu, Y. H. Feng and H. Y. Chen, *Angew. Chem., Int. Ed.*, 2020, **59**, 22246–22251.

32 S. Mubeen, J. Lee, N. Singh, S. Krämer, G. D. Stucky and M. Moskovits, *Nat. Nanotechnol.*, 2013, **8**, 247–251.

33 B. H. Wu, D. Y. Liu, S. Mubeen, T. T. Chuong, M. Moskovits and G. D. Stucky, *J. Am. Chem. Soc.*, 2016, **138**, 1114–1117.

34 H. L. Jia, A. X. Du, H. Zhang, J. H. Yang, R. B. Jiang, J. F. Wang and C.-y. Zhang, *J. Am. Chem. Soc.*, 2019, **141**, 5083–5086.

35 H. L. Jia, F. Li, T. H. Chow, X. Y. Liu, H. Zhang, Y. Lu, J. F. Wang and C.-y. Zhang, *Nano Lett.*, 2022, **22**, 7268–7274.

36 X. Q. Yang, Y. Liu, S. H. Lam, J. Wang, S. Z. Wen, C. Yam, L. Shao and J. F. Wang, *Nano Lett.*, 2021, **21**, 8205–8212.

37 M. T. Chen, Z. J. Ye, L. Wei, J. Yuan and L. H. Xiao, *J. Am. Chem. Soc.*, 2022, **144**, 12842–12849.

38 G. L. He, Y. H. Lai, Y. Z. Guo, H. Yin, B. B. Chang, M. Liu, S. R. Zhang, B. C. Yang and J. F. Wang, *ACS Appl. Mater. Interfaces*, 2022, **14**, 53724–53735.

39 H. Zhang, S. H. Lam, Y. Z. Guo, J. H. Yang, Y. Lu, L. Shao, B. C. Yang, L. H. Xiao and J. F. Wang, *ACS Appl. Mater. Interfaces*, 2021, **13**, 51855–51866.

40 B. T. Sneed, C.-H. Kuo, C. N. Brodsky and C.-K. Tsung, *J. Am. Chem. Soc.*, 2012, **134**, 18417–18426.

41 C. Y. Yang, B. L. Huang, S. X. Bai, Y. G. Feng, Q. Shao and X. Q. Huang, *Adv. Mater.*, 2020, **32**, 2001267.

42 Y.-Q. Kang, Q. Xue, Y. Zhao, X.-F. Li, P.-J. Jin and Y. Chen, *Small*, 2018, **14**, 1801239.

43 C. Zhang, H. Q. Zhao, L. N. Zhou, A. E. Schlather, L. L. Dong, M. J. McClain, D. F. Swearer, P. Nordlander and N. J. Halas, *Nano Lett.*, 2016, **16**, 6677–6682.

44 F. Wang, C. H. Li, H. J. Chen, R. B. Jiang, L.-D. Sun, Q. Li, J. F. Wang, J. C. Yu and C.-H. Yan, *J. Am. Chem. Soc.*, 2013, **135**, 5588–5601.

45 L. N. Zhou, D. F. Swearer, C. Zhang, H. Robatjazi, H. Q. Zhao, L. Henderson, L. L. Dong, P. Christopher, E. A. Carter, P. Nordlander and N. J. Halas, *Science*, 2018, **362**, 69–72.

46 S. K. Cushing, J. T. Li, F. K. Meng, T. R. Senty, S. Suri, M. J. Zhi, M. Li, A. D. Bristow and N. Q. Wu, *J. Am. Chem. Soc.*, 2012, **134**, 15033–15041.

47 J. T. Li, S. K. Cushing, F. K. Meng, T. R. Senty, A. D. Bristow and N. Q. Wu, *Nat. Photonics*, 2015, **9**, 601–607.

48 H. Robatjazi, H. Q. Zhao, D. F. Swearer, N. J. Hogan, L. N. Zhou, A. Alabastri, M. J. McClain, P. Nordlander and N. J. Halas, *Nat. Commun.*, 2016, **8**, 27.

49 P. Christopher, H. L. Xin, A. Marimuthu and S. Linic, *Nat. Mater.*, 2012, **11**, 1044–1050.

50 P. Christopher, H. L. Xin and S. Linic, *Nat. Chem.*, 2011, **3**, 467–472.

51 S. Mukherjee, F. Libisch, N. Large, O. Neumann, L. V. Brown, J. Cheng, J. B. Lassiter, E. A. Carter, P. Nordlander and N. J. Halas, *Nano Lett.*, 2013, **13**, 240–247.

52 J. H. Yang, Y. Z. Guo, W. Z. Lu, R. B. Jiang and J. F. Wang, *Adv. Mater.*, 2018, **30**, 1802227.

53 H. Yin, J. W. Hu, C. H. Fang, Y. Y. Wang, L. X. Ma, N. Zhang, S. R. Zhang, R. B. Jiang and J. F. Wang, *Nano Res.*, 2023, **16**, 360–370.